

This work was written as part of one of the author's official duties as an Employee of the United States Government and is therefore a work of the United States Government. In accordance with 17 U.S.C. 105, no copyright protection is available for such works under U.S. Law.

Public Domain Mark 1.0

<https://creativecommons.org/publicdomain/mark/1.0/>

Access to this work was provided by the University of Maryland, Baltimore County (UMBC) ScholarWorks@UMBC digital repository on the Maryland Shared Open Access (MD-SOAR) platform.

**Please provide feedback**

Please support the ScholarWorks@UMBC repository by emailing [scholarworks-group@umbc.edu](mailto:scholarworks-group@umbc.edu) and telling us what having access to this work means to you and why it's important to you. Thank you.



# Delayed Development of Cool Plasmas in X-Ray Flares from the Young Sun-like Star $\kappa^1$ Ceti

Kenji Hamaguchi<sup>1,2</sup> , Jeffrey W. Reep<sup>3</sup> , Vladimir Airapetian<sup>4,5</sup> , Shin Toriumi<sup>6</sup> , Keith C. Gendreau<sup>7</sup> , and Zaven Arzoumanian<sup>7</sup>

<sup>1</sup> CRESST II and X-ray Astrophysics Laboratory, NASA/GSFC, Greenbelt, MD 20771, USA; [kenji.hamaguchi@umbc.edu](mailto:kenji.hamaguchi@umbc.edu)

<sup>2</sup> Department of Physics, University of Maryland, Baltimore County, 1000 Hilltop Circle, Baltimore, MD 21250, USA

<sup>3</sup> Space Science Division, US Naval Research Laboratory, Washington, DC 20375, USA

<sup>4</sup> American University, 4400 Massachusetts Avenue NW, Washington, DC 20016 USA

<sup>5</sup> NASA/GSFC/SEEC, Greenbelt, MD 20771, USA

<sup>6</sup> Institute of Space and Astronautical Science, Japan Aerospace Exploration Agency, 3-1-1 Yoshinodai, Chuo-ku, Sagami-hara, Kanagawa, 252-5210, Japan

<sup>7</sup> X-Ray Astrophysics Laboratory, NASA/GSFC, Greenbelt, MD 20771, USA

Received 2022 July 18; revised 2022 December 2; accepted 2022 December 21; published 2023 February 22

## Abstract

The Neutron star Interior Composition Explorer (NICER) X-ray observatory observed two powerful X-ray flares equivalent to superflares from the nearby young solar-like star  $\kappa^1$  Ceti in 2019. NICER follows each flare from the onset through the early decay, collecting over 30 counts  $\text{s}^{-1}$  near the peak, enabling a detailed spectral variation study of the flare rise. The flare in September varies quickly in  $\sim 800$  s, while the flare in December has a few times longer timescale. In both flares, the hard-band (2–4 keV) light curves show typical stellar X-ray flare variations with a rapid rise and slow decay, while the soft X-ray light curves, especially of the September flare, have prolonged flat peaks. The time-resolved spectra require two temperature plasma components at  $kT \sim 0.3$ –1 and  $\sim 2$ –4 keV. Both components vary similarly, but the cool component lags by  $\sim 200$  s with a four to six times smaller emission measure (EM) compared to the hot component. A comparison with hydrodynamic flare loop simulations indicates that the cool component originates from X-ray plasma near the magnetic loop footpoints that mainly cools via thermal conduction. The time lag represents the travel time of the evaporated gas through the entire flare loop. The cool component has a several times smaller EM than its simulated counterpart, suggesting a suppression of conductive cooling, possibly by the expansion of the loop cross-sectional area or turbulent fluctuations. The cool component's time lag and EM ratio provide important constraints on the flare loop geometry.

*Unified Astronomy Thesaurus concepts:* Main sequence stars (1000); Solar analogs (1941); Stellar flares (1603); Stellar x-ray flares (1637)

## 1. Introduction

Solar and stellar flares are the most energetic events on low-mass stars (Haisch et al. 1991; Güdel & Nazé 2009). They represent the rapid conversion of the magnetic energy of active regions into kinetic and thermal energies, radiating from radio to gamma rays and ejecting high-energy nuclei and electrons. Powerful solar flares have disrupted the Earth's magnetosphere and human activity, yet flares of young Sun-like stars can far surpass their solar counterparts in energy and frequency, with their enhanced magnetic dynamos driven by rapid rotations and deep convections. Their intense radiation could impact the exoplanetary environment and habitability (e.g., Airapetian et al. 2020).

These flares, even with substantial energy variations, share similar behavior and characteristics and arise from the universal magnetic reconnection mechanism. Magnetic reconnection efficiently accelerates particles to high energies ( $\gtrsim 10$  keV), which bombards the footpoints of the loops with high-energy particles and heats the chromosphere; the evaporated gas fills the magnetic loop and gradually cools down via radiation. The evaporated gas at  $\approx 10^7$  K radiates primarily in soft X-rays between 0.1 and 10 keV ( $\approx 1$ –100 Å). Therefore, soft X-ray

observations are crucial in understanding the flare geometry and heating mechanisms.

During a typical flare, soft X-ray emission rises quickly as the evaporated gas fills the magnetic loop and decays quasi-exponentially as it gradually cools down radiatively. Earlier studies have focused on the peak and decay phase of flares (White et al. 1986; van den Oord & Mewe 1989; Reale & Micela 1998; Tsuboi et al. 1998; Favata et al. 2000; Sasaki et al. 2021). They suggested that powerful flares tend to decay slowly and originate from larger flare loops, which exceed the stellar radius in extreme cases. Direct solar flare imagings, stellar flare occultation observations, or theoretical models support this idea, but the models can significantly overestimate the flare size due to continuous heating, multiple loop structures, or subsequent flares during the decay phase (e.g., Schmitt & Favata 1999; Güdel et al. 2004; Reep & Toriumi 2017; Toriumi et al. 2017).

The rising phase holds crucial information on the flare geometry and heating mechanism (e.g., Reale 2007) as it goes through initial heating, evaporation, and loop filling. However, the rising phase is often shorter than the decaying phase (e.g., Reep & Knizhnik 2019; Getman et al. 2021), so it has been mostly limited to duration or crude hardness ratio studies in the soft X-ray band. An exception is an XMM-Newton observation of Proxima Centauri, which caught a bright flare from the onset to the middle of the decay, recording  $\gtrsim 100$  counts  $\text{s}^{-1}$  near the peak (Güdel et al. 2002, 2004; Reale et al. 2004). The X-ray



Original content from this work may be used under the terms of the [Creative Commons Attribution 4.0 licence](https://creativecommons.org/licenses/by/4.0/). Any further distribution of this work must maintain attribution to the author(s) and the title of the work, journal citation and DOI.

hardness ratio reached its maximum in the middle of the rise and started to decline near the flux peak. The timing of the maximum hardness coincides with the  $U$ -band (3000–3900 Å) flux peak measured with the onboard Optical Monitor, suggesting a connection between the coronal and chromospheric heating.

The Neutron star Interior Composition ExploreR (NICER) X-ray observatory on board the International Space Station (ISS; Gendreau & Arzoumanian 2017) observed two bright X-ray flares from the nearby solar-like star  $\kappa^1$  Ceti (aka HD 20630, HIP 15457;  $d=9.16$  pc, mass =  $1.04 M_{\odot}$ , radius =  $0.95 \pm 0.10 R_{\odot}$ , effective temperature = 5665 K; Rucinski et al. 2004; Ribas et al. 2010) during a monitoring program for the Sellers Exoplanet Environments Collaboration<sup>8</sup> in 2019. This star shows intense magnetic activity due to its fast stellar rotation ( $P=9.2$  days), emitting 2 orders of magnitude higher coronal X-rays and chromospheric UV light than the Sun. In 1986, the star showed a signature of a superflare event in the He I D3 ( $\lambda 5875.6$  Å) optical line, with an estimated total flare energy of  $E \approx 2 \times 10^{34}$  erg (Schaefer et al. 2000). Still, the radiation from the transition region and coronal plasma satisfies a solar magnetic flux scaling law similar to other Sun-like stars (Toriumi & Airapetian 2022). These characteristics suggest that  $\kappa^1$  Ceti is a young solar analog at 0.4–0.8 Gyr old with an enhanced solar-type coronal and chromospheric heating rates (Airapetian et al. 2021). Its global-scale magnetic shear may cause superflares that eject huge masses of coronal material (Lynch et al. 2019).

The NICER X-ray observatory primarily aims at studying rapidly rotating neutron stars with very high timing resolution, but its superb soft X-ray collecting power, wide dynamic range, high throughput, moderate background, decent energy resolution, tolerance to optical light, and rapid maneuvering capability make it a powerful tool for observing nearby solar-type stars with sporadic bright X-ray flares. This paper describes an analysis of NICER observations of the two powerful X-ray flares from  $\kappa^1$  Ceti and performs hydrodynamic simulations of single loop flares to interpret the observations. The result shows how X-ray plasmas develop during the flare rising phase in detail.

## 2. Observation

The NICER X-ray Timing Instrument (XTI) is an array of 56 aligned X-ray modules, each of which consists of an X-ray concentrator (XRC; Okajima et al. 2016) and a silicon drift detector (SDD; Prigozhin et al. 2016). Each XRC concentrates X-rays within an  $\sim 3'$  radius field of view to the paired SDD, which detects each photon with an accuracy of  $\sim 84$  ns. The XTI as a whole has one of the largest collecting areas among X-ray instruments between 0.2 and 12 keV ( $\sim 1900 \text{ cm}^2$  at 1.5 keV). We use 50 XTI modules, as the remaining six (IDs 11, 14, 20, 22, 34, and 60) are inactive or noisy.

NICER can continuously observe a target up to  $\sim 2.5$  ks in every ISS orbit ( $\sim 5.5$  ks). However, target visibility can be limited by Earth or ISS structure occultation or proximity to high-particle regions such as the South Atlantic Anomaly. NICER can quickly slew the telescope and so observes multiple targets in each ISS orbit to maximize the observing efficiency. This capability enables NICER to visit a target

frequently, but it can also cause scheduling conflicts with other timely targets.

NICER started monitoring  $\kappa^1$  Ceti on 2019 September 16; it observed the star for  $\sim 180$  ks between 2019 and 2021. During these monitoring observations, NICER detected two prominent X-ray flares on 2019 September 17 and December 10. Earlier X-ray imaging observations did not detect any X-ray sources at significant X-ray brightness within  $3'$  of  $\kappa^1$  Ceti (e.g., Telleschi et al. 2005), indicating that the flares originate from  $\kappa^1$  Ceti.

We analyze NICER ObsIDs 2300020101, 2300020102, and 2300020114. We reprocess the data sets with NICER calibration ver. CALDB XTI(20210707) using `nicerl2` in HEASoft ver. 6.29c and NICERDAS ver. V008c. We evaluate the particle background using `nibackgen3C50` ver. v7b with the parameters `dtmin = 10.0`, `dtmax = 60.0`, `hbgsut = 0.1`, and `s0cut = 30.0` (Remillard et al. 2022). We use `python` ver. 3.7, `numpy` ver. 1.20.3, `scipy` ver. 1.1.0, and `astropy` ver. 3.1.

## 3. Observation Results

### 3.1. Light Curves

The first flare occurred on 2019 September 17, during the last snapshot of the 1 day observation of  $\kappa^1$  Ceti from September 16 (190917; Figure 1, top). The snapshot only lasts for  $\sim 800$  s, but it covers the rise and beginning of the decay of the flare, as the flare varies very quickly. The Bayesian block analysis tool, `bayesian_blocks` in the `astropy` package (Scargle et al. 2013)—a nonparametric statistical analysis to detect significant flux change in time-series data—does not suggest that the 0.6–1.2 keV count rate changes from the previous snapshot to the first 100 s of this snapshot. This result suggests that the flare begins around the boundary of the last snapshot’s second and third time bins, 2019 September 17 at 9<sup>h</sup>36<sup>m</sup>52<sup>s</sup> UT.

Figure 2 (left) shows band-sliced light curves of the last snapshot. The 2–4 keV light curve is typical of solar and stellar X-ray flares (Benz & Güdel 2010, and references therein), showing a sharp rise in  $\sim 200$  s and a steady decline by a factor of 3 in  $\sim 500$  s after the peak. However, the softer-band light curves rise more slowly, peak later, and decay more gradually. The light curves below 1.2 keV may not even show a decay during the snapshot. The soft-band light curves significantly deviate from the hard-band light curves. The hardness ratio in the bottom panel rises quickly, peaks before the total (0.3–4 keV) light curve, and declines gradually. This behavior is similar to the giant flare seen from Proxima Centauri with XMM-Newton (Güdel et al. 2004).

The second flare occurred during the second snapshot on 2019 December 10 (191210; Figure 1, bottom). This observation ( $\sim 1.6$  ks) is longer than for the first flare, but it similarly covers the rise and beginning of the decay, as the second flare develops more slowly. NICER misses the middle of the decay, but the third snapshot covers the end of the decay, as the light curve connects smoothly from the second snapshot. On the other hand, the first snapshot shows a slight elevation in the middle, but both intervals appear to be in a quiescent state without significant variation. The light curve before the first flare also shows similar count rate variations (Figure 1, top). A Bayesian block analysis shows that the 0.6–1.2 keV count rate stays at  $\sim 6.6 \text{ counts s}^{-1}$  from the latter half of the first snapshot to the first  $\sim 150$  s of the second snapshot, suggesting that the flare begins during the second snapshot at around 19<sup>h</sup>14<sup>m</sup>40<sup>s</sup>

<sup>8</sup> <https://seec.gsfc.nasa.gov>

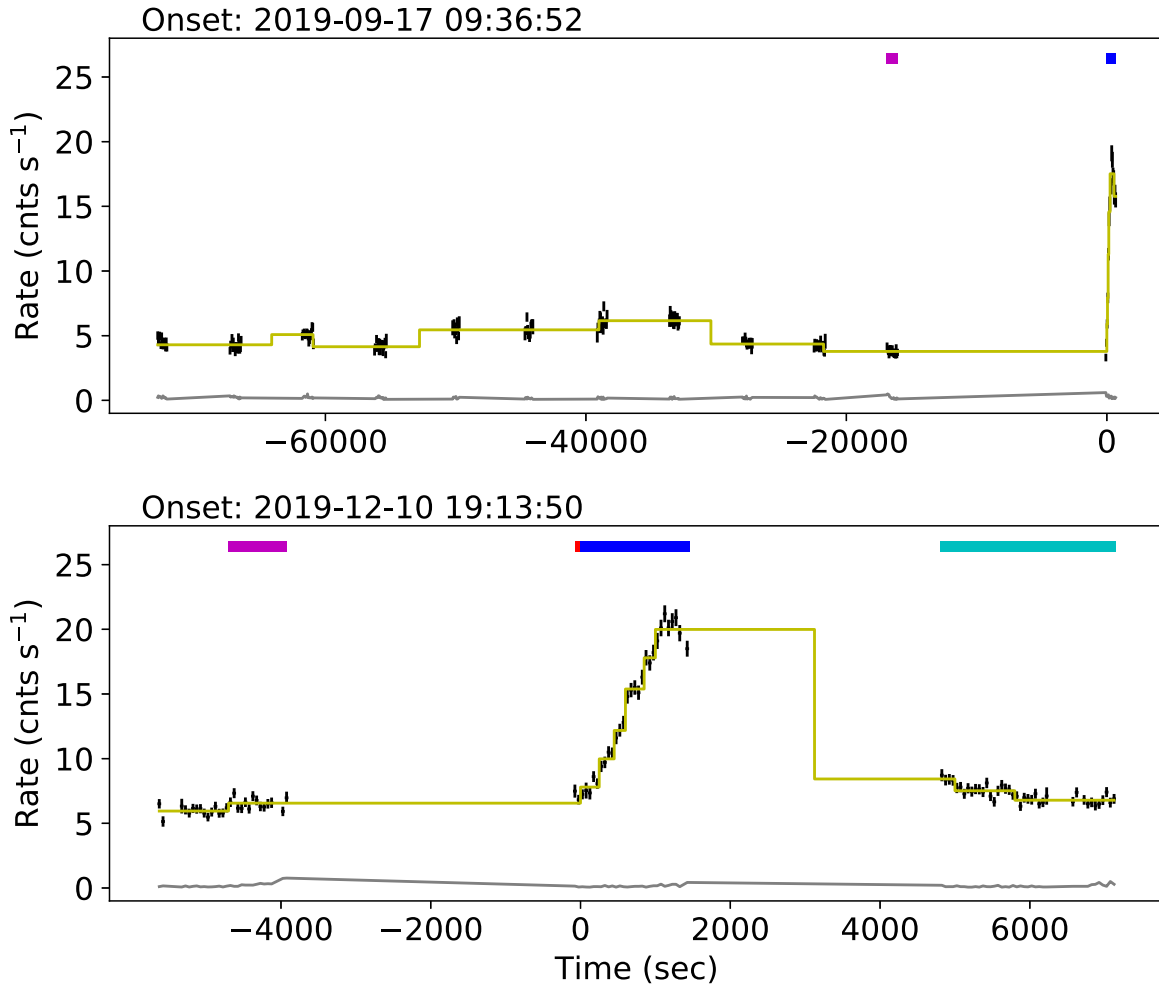


**Figure 1.** Background-subtracted light curves of  $\kappa^1$  Ceti between 0.6 and 1.2 keV on 2019 September 16–17 (top) and 2019 December 10 (bottom). NICER opportunely caught the rising phase of a bright X-ray flare during each observation. The gray and yellow lines show the background level estimated with the NICER tool `nibackgen3C50` and an average count of each Bayesian block derived with the `astropy` tool `bayesian_blocks`. The time on the top shows the light-curve origin, an estimated flare onset. The color bars present quiescent (magenta), preflare (red), flare rise and peak (blue), and flare decay end (cyan) intervals for the spectral analysis. Each data bin is 50 s.

UT. Meanwhile, the last Bayesian block of the third snapshot has almost the same count rate ( $\sim 6.8$  counts  $s^{-1}$ ), suggesting that the quiescent emission does not vary significantly during the flare.

Besides the slow variation, the second flare has similar energy-dependent variations as the first flare. The 2–4 keV light curve reaches its peak before other energy bands. The softer band peaks are delayed; the 0.3–0.6 keV light curve does not show a clear peak during the second snapshot. This delay continues to the third snapshot. The softer-band light curves gradually decline, while the 2–4 keV light curve is almost flat. The hardness ratio reaches a maximum early during the rise, but otherwise, the variation is similar to the first flare.

### 3.2. Time-resolved Spectra

To understand the energy-dependent time variations, we analyze the time-resolved spectra. We first produce a quiescent spectrum from the snapshot directly preceding each flare (the magenta bar in Figure 1). The snapshot of the September flare shows no significant variation in count rate, while that in December does show a small but significant count rate increase in the middle at  $-4.7$  ks (Figure 1, bottom). Therefore, we produce two spectra separated at the time with a statistically

significant count rate change (change point) in the Bayesian analysis (Figure 3). The quiescent spectra show a prominent hump between 0.7 and 0.9 keV, consistent with emission lines of Fe XVII–XX, Ne IX–X, and O VIII ions seen in the XMM-Newton RGS spectra of  $\kappa^1$  Ceti in 2002 (Telleschi et al. 2005). The spectrum has a steep hard slope, with negligible emission above  $\sim 2$  keV but no absorption cutoff in the soft band down to 0.3 keV. We thus apply a thermal plasma emission model (`appec`) without absorption (Table 1). Assuming the best-fit elemental abundances of the XMM/RGS spectrum (Appendix), we find that a two-temperature (2T) model with  $kT = 0.27$  and 0.62 keV provides an acceptable fit to the quiescent spectrum for the September flare. The quiescent spectra of the December flare require a 3T model for the former interval and an additional 1T component for the latter interval to account for the flux increase. We use this 4T model as the fixed quiescent component for the December flare spectra.

We produce time-resolved spectra during the flares every 50 s with a minimum 25 counts  $bin^{-1}$  for the September flare to track the fast variation and every 100 s with a minimum of 50 counts  $bin^{-1}$  for the December flare to get good photon statistics (Figures 4 and 5). For each flare, we make one spectrum before the flare onset in the same snapshot (the red

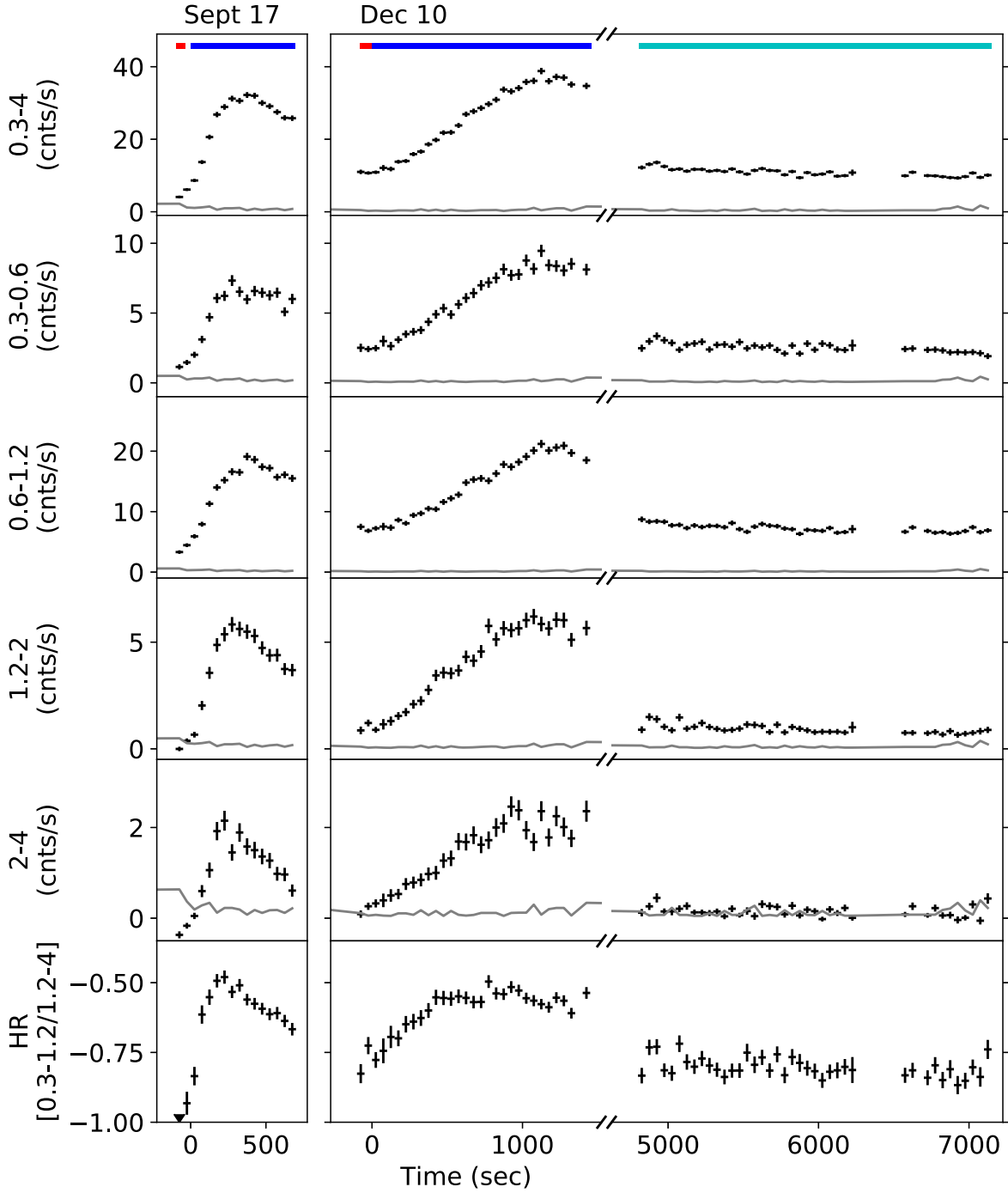


**Figure 2.** First–fifth rows: band-sliced light curves of  $\kappa^1$  Ceti around the first flare on 2019 September 17 (left) and the second flare on December 10 (right). These light curves have the same horizontal scales, so the variation timescales are directly comparable. The soft-band light curves in the upper panels have delayed peaks compared with the 2–4 keV light curve. The gray line shows the instrumental background level. Each light curve has 50 s bins. Sixth row: time series of the hardness ratio defined by  $(H - S)/(H + S)$ , where  $H$  and  $S$  are the net count rates between 1.2–4 and 0.3–1.2 keV, respectively. The color bars present preflare (red), flare rise and peak (blue), and flare decay end (cyan) intervals for the spectral analysis. The first bin of the September flare is below  $-1$ , as `nibackgen3C50` overestimates the hard-band background. In each flare, the hardness ratio peaks before the total (0.3–4 keV) band count rate maximum.

bars in Figure 2 between  $-95$  and  $-35$  s for the first flare and  $-80$  and  $0$  s for the second flare), which we call the preflare spectrum. In the third snapshot of the December flare, due to a decreased count rate, we increase the time interval of each bin to 400–600 s. We also apply longer time intervals for the third snapshot of the December flare near the decay end. The preflare spectrum in the top left panel of each figure matches well the corresponding quiescent spectrum (solid yellow line), consistent with the Bayesian block analysis of the flare onset timings.

During the first flare, the flux in the entire energy band increases for the first 300 s. The 0.7–0.9 keV hump becomes broader to the high-energy side as the flux at  $\sim 1.1$  keV, probably originating from Fe XXII–XXIV or Ne X emission lines, is enhanced. After that, the hard-band emission gradually declines, while the flux at  $\sim 0.9$  keV, probably produced by Fe XVII–XX lines, strengthens. The second flare evolves more slowly but similarly to the first flare. The whole band increases until  $\sim 800$  s, and then the hump at  $\sim 0.9$  keV begins to



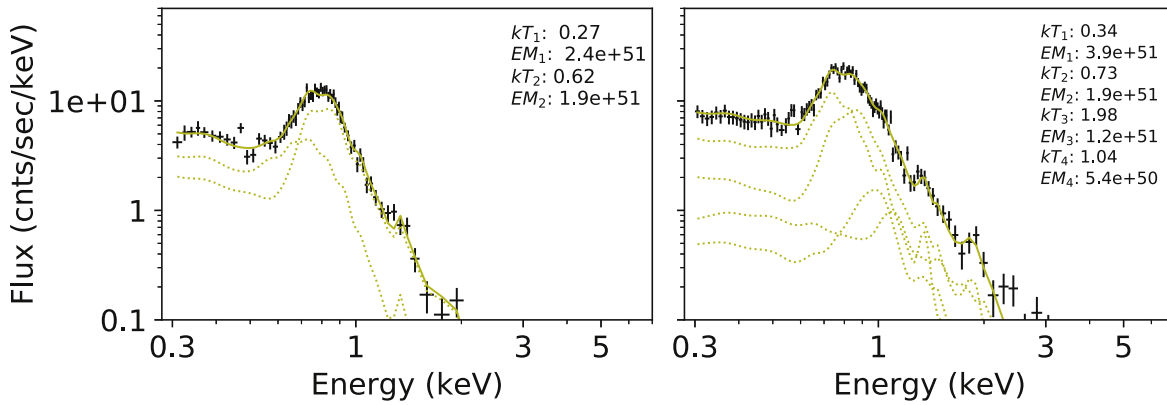


**Figure 3.** Quiescent spectra of the first flare for an exposure of 870 s from  $-16,921$  to  $-16,051$  s (left) and the second flare for 789 s from  $-4700$  to  $-3911$  s (right). The solid yellow lines are the best-fit models, and the dotted lines are the individual components. The upper right corner of each panel shows the best-fit parameters (the units are keV for  $kT$  and  $\text{cm}^{-3}$  for EM). The best-fit models reproduce the observed spectra well.

**Table 1**  
Best-fit Values of the Quiescent Spectra

Component	190917		191210	
	$kT$ (keV)	EM ( $10^{51} \text{ cm}^{-3}$ )	$kT$ (keV)	EM ( $10^{51} \text{ cm}^{-3}$ )
1	$0.27^{+0.03}_{-0.03}$	$2.4^{+0.4}_{-0.4}$	$0.34^{+0.02}_{-0.03}$	$3.9^{+0.4}_{-0.6}$
2	$0.62^{+0.04}_{-0.03}$	$1.9^{+0.3}_{-0.4}$	$0.73^{+0.06}_{-0.06}$	$1.9^{+0.5}_{-0.4}$
3			$1.98^{+0.87}_{-0.38}$	$1.2^{+0.2}_{-0.5}$
4			$1.04^{+0.29}_{-0.20}$	$0.5^{+1.1}_{-0.2}$
$\Delta\chi^2/\text{d.o.f.}$	55.44/64		162.06/175	

**Note.** The errors show 90% confidence ranges. The fourth component is required for the latter interval spectrum of the 191210 observation.

strengthen. In the third snapshot, the flux declines nearly to the preflare level, with some residual in the soft and hard bands in the prior  $\sim 1$  ks.

### 3.3. $kT$ and EM Variations during the Flares

The time-resolved spectra do not suggest any significant variation of the quiescent component during the flares. We therefore reproduce each time-resolved spectrum by a model with variable flare components plus the fixed quiescent component. The hard slopes of most spectra require  $kT \sim 3$  keV plasma. However, collisional equilibrium plasma at that temperature does not emit Fe XVII–XX emission lines at  $\sim 0.9$  keV, which are enhanced near the flare peaks. Nonequilibrium ionization plasmas emit these lines at  $\tau \sim 2 \times 10^{10} \text{ s cm}^{-3}$ , but they do not reproduce the emission lines at  $\sim 1.1$  keV observed during the rising phase. This result suggests that the flare spectra need at least two plasma components. We thus apply a  $2T_{\text{apec}}$  plasma model for the flare emission, with elemental abundances fixed to the best-fit XMM/RGS values. We find that a model with  $kT \sim 2$ –4 and 0.3–1 keV components reproduces each spectrum well, and that these temperatures vary monotonically over time. However, the spectral parameters are poorly constrained near the flare onset and end due to weak flare emission. We therefore fit all spectra simultaneously, assuming that each component’s plasma temperature varies linearly with time, and find reasonable results with  $\chi^2/\text{d.o.f.}$  at 685.96/616 for the first flare and 1118.41/919 for the second flare. Figures 4 and 5 plot the best-

fit model for individual spectra, and Figure 6 shows the best-fit  $kT$  and EM values. The third and fourth columns in Table 2 show the best-fit  $kT$  slopes.

The cool-component EMs are mainly determined by fits of the Fe L emission line complex to the  $\sim 0.9$  keV excess. We examine whether the line intensity constraints in the applied model are adequate for this analysis. First, the model fixes the elemental abundances during the flares at the best-fit XMM/RGS quiescent spectrum values. However, some solar or stellar X-ray flares show apparent elemental abundance changes from the pre- or postflare states (e.g., Osten et al. 2000; Audard et al. 2001; Mondal et al. 2021). The best-fit spectral models also fit well the  $\sim 1.1$  keV bump with the Fe L and Ne K lines in the hot component. Since the hard spectral slope determines the hot component’s EM, the hot component’s Fe and Ne abundances are consistent with the assumed abundances; i.e., the coronal abundances are not observed to significantly change during the  $\kappa^1$  Ceti flares. Second, suppose the cool component did not reach equilibrium at ionization timescales of  $\lesssim 10^{10} \text{ s cm}^{-3}$  as opposed to the model assumption. In that case, the plasma should emit weaker Fe L lines than the equilibrium case and require a larger EM to account for the observed 1.1 keV bump. However, no observed spectra show the strong emission below  $\sim 0.7$  keV expected from low ionized oxygen and carbon emission lines from such nonequilibrium plasmas. In addition, the preflare loops probably have densities over  $\sim 10^{11} \text{ cm}^{-3}$  (e.g., Osten et al. 2006), suggesting that the Fe L line complex develops within  $\approx 0.1$  s. These results suggest that the cool-component EM measurements are robust.

The hot component explains most of the initial flux rise in each flare. The component in the second flare is slightly hotter and cools down significantly slower than the first flare, but the component stays  $kT \gtrsim 2$  keV throughout both observations. On the other hand, the cool component develops more slowly than the hot component. The plasma temperature does not vary strongly at  $\sim 1$  keV around the flare peak, but it declines to  $\sim 0.3$  keV by the end of the second flare.

The EM time series in Figure 6 (bottom panels) confirms the similarity of the two flares: (i) the hot EM varies with a linear rise and a slow decay, and (ii) the cool EM varies similarly to the hot EM but with a delay. To quantitatively evaluate their variations, we fit the EM time series with the following

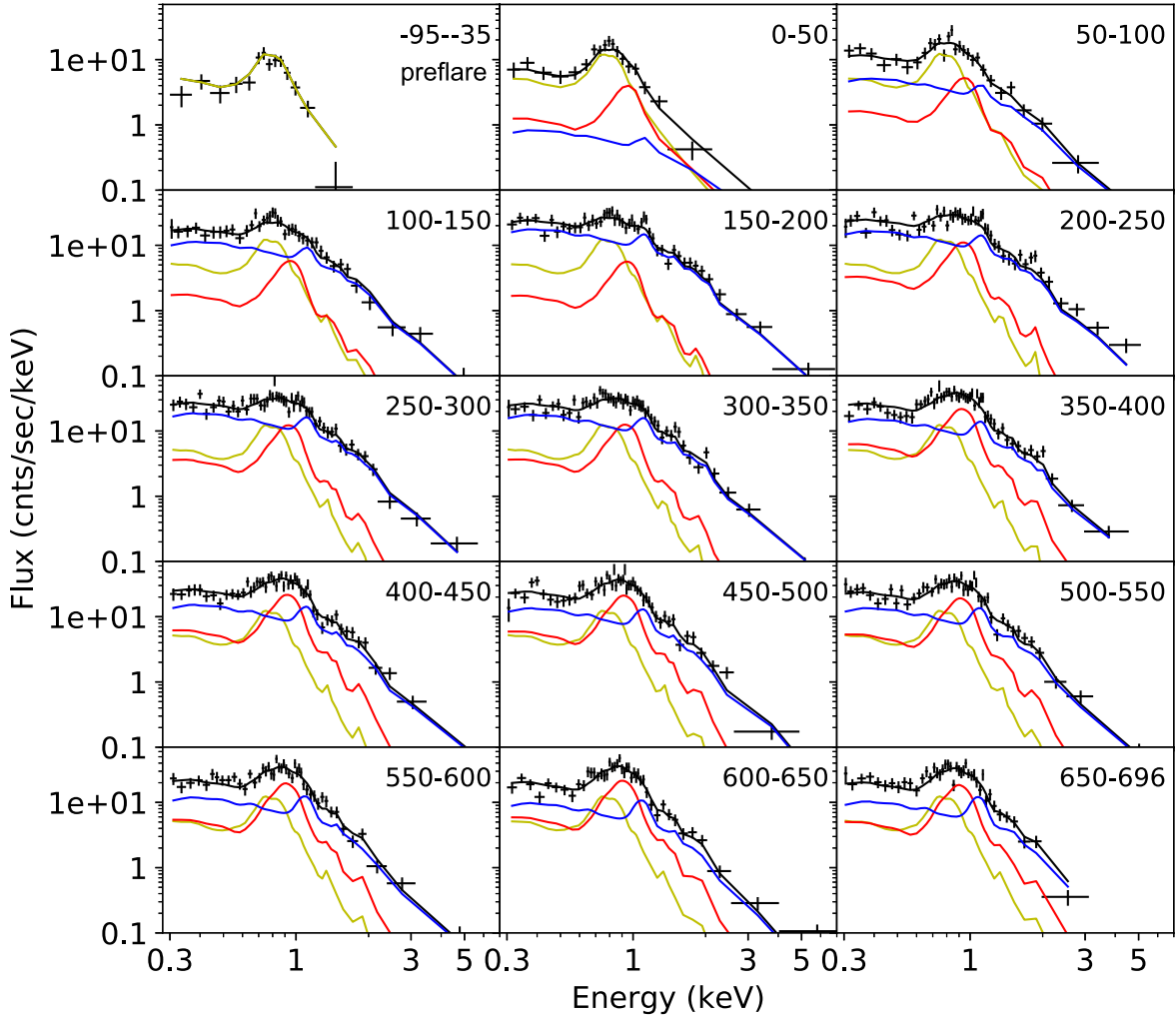


**Figure 4.** Time-resolved spectra of  $\kappa^1$  Ceti during the first flare (190917). The red/blue line depicts the best-fit cool/hot component of the flare spectrum, and the yellow line does the fixed quiescent component. The solid black line is their sum. The hot component soars in the rising phase, dominating most energy bands, while the cool component is more significant at  $\sim 0.9$  keV with Fe L emission lines after  $\sim 350$  s. The top right corner of each panel shows each spectrum's time interval in seconds.

conventional formula for stellar flares:

$$\begin{aligned}
 \text{EM}(t) &= 0 & t < t_{\text{onset}} \\
 &= \text{EM}_{\text{peak}} \frac{t - t_{\text{onset}}}{\Delta t_{\text{rise}}} & t_{\text{onset}} \leq t < t_{\text{peak}} \\
 &= \text{EM}_{\text{peak}} \exp\left(-\frac{t - t_{\text{peak}}}{\tau_{\text{decay}}}\right) & t_{\text{peak}} \leq t,
 \end{aligned} \quad (1)$$

where  $t_{\text{onset}}$ ,  $t_{\text{peak}}$ ,  $\text{EM}_{\text{peak}}$ , and  $\tau_{\text{decay}}$  are free parameters, and  $\Delta t_{\text{rise}} = t_{\text{peak}} - t_{\text{onset}}$ . For the fittings, we use `curve_fit` in the `scipy` package. We fix the  $\Delta t_{\text{rise}}$  and  $\tau_{\text{decay}}$  of the 190917 flare's cool component at the best-fit values of the hot component, as the cool component does not show a clear EM peak. Table 2 shows the best-fit result. The hot component's  $t_{\text{onset}}$  is close to zero, again consistent with the Bayesian block measurement of the flare onset in each flare. In contrast, the cool component's  $t_{\text{onset}}$  is significantly delayed from the hot component's  $t_{\text{onset}}$  (hereafter  $\Delta t_{\text{delay}} = t_{\text{onset}}(\text{cool}) - t_{\text{onset}}(\text{hot})$ ). In the second flare, the cool component has a similar  $\Delta t_{\text{rise}}$  to but a factor of 2 longer  $\tau_{\text{decay}}$  than the hot component. The

second flare has longer durations in  $\Delta t_{\text{delay}}$ ,  $\Delta t_{\text{rise}}$ , and  $\tau_{\text{decay}}$  than the first flare.

These behaviors explain the energy-dependent variations of the light curves. The 2–4 keV band light curve is dominated by the hot component's behavior, showing a conventional stellar flare variation. The softer bands add the cool component's behavior with a conventional flare variation but a time delay compared to the hot component. The 0.6–1.2 keV light curve deviates most with the strong 0.9 keV hump from the cool component. The deviation is stronger in the first flare with a larger relative time delay ( $\Delta t_{\text{delay}}/\Delta t_{\text{rise}}$ ) and a larger  $\text{EM}_{\text{peak}}(\text{cool})/\text{EM}_{\text{peak}}(\text{hot})$  ratio.

#### 4. Hydrodynamic Simulations of Single Loop Flares

The hot component constitutes the major part of the flare emission. As discussed in numerous studies, it should originate from radiatively cooling plasma inside the flare magnetic loops. Then, what is the cool component? Flare spectral fits often require two temperatures or more (e.g., Paudel et al. 2021; Sasaki et al. 2021), but the nature of the cool component is poorly known. Our NICER study provides this component's

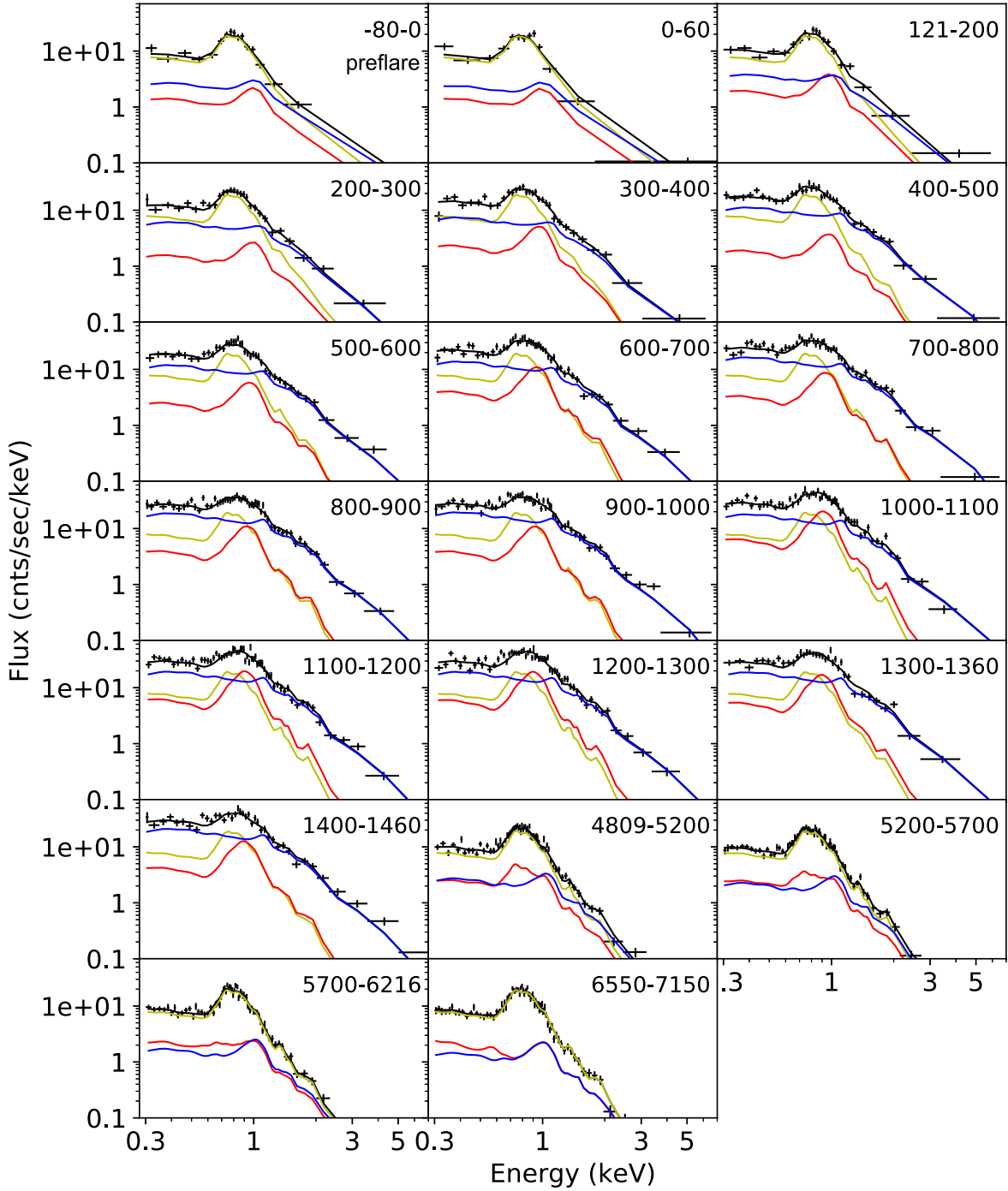


**Figure 5.** Time-sliced spectra of  $\kappa^1$  Ceti during the second flare (191210). The flare spectral components behave similarly to those of the first flare. The cool component exceeds the hot component at  $\sim 0.9$  keV after  $\sim 1$  ks, but not as much as during the first flare.

time variation through the flare rise. We run hydrodynamic simulations of single magnetic loop flares to understand the cool component.

We employ a field-aligned hydrodynamic code, the HYDrodynamics and RADiation code (HYDRAD;<sup>9</sup> Bradshaw & Mason 2003), used to study heating in the solar corona and solar flares. The code solves the equations for the conservation of mass, momentum, and energy for plasma confined to a magnetic flux tube (Bradshaw & Cargill 2013). The loops are assumed to be heated by nonthermal electrons, accelerated by

magnetic reconnection near the loop’s apex. As the electrons propagate, they deposit their energy through Coulomb collisions with the ambient plasma. The majority of the heat is deposited in the upper chromosphere, causing a rapid increase in temperature and pressure. It then drives an expansion of material (chromospheric evaporation), carrying hot and dense plasma into the corona. The assumed form of the heating function that we use was derived by Emslie (1978), with modification for nonuniform ionization in the chromosphere (Hawley & Fisher 1994). As the loop evolves, the plasma cools through thermal conduction and radiation, which we calculated using the atomic database CHIANTI (Dere et al. 1997), version

<sup>9</sup> <https://github.com/rice-solar-physics/HYDRAD>



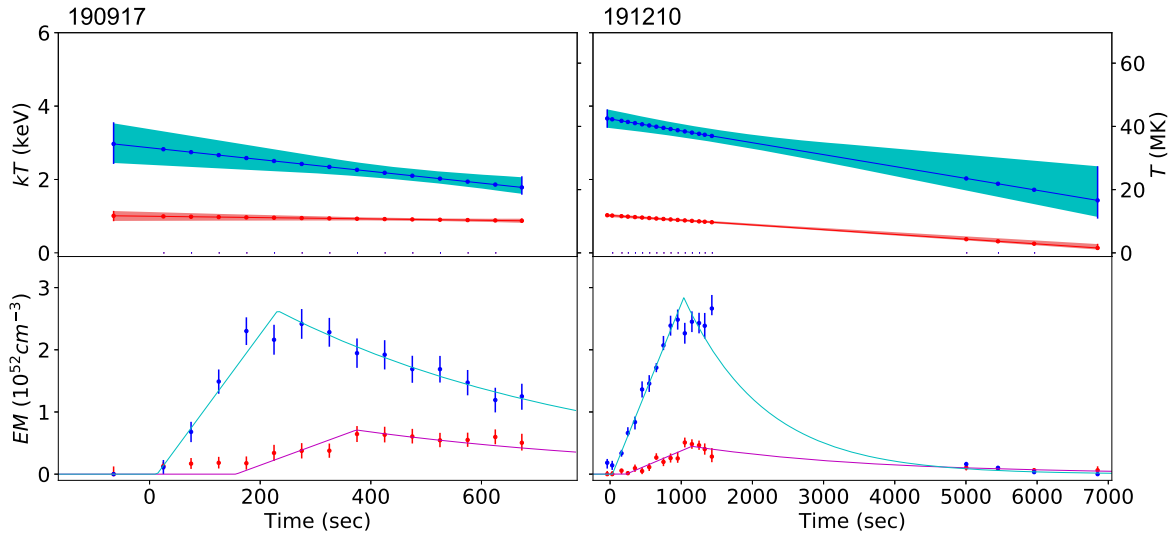


**Figure 6.** Best-fit  $kT$  (top) and EM (bottom) values of the time-resolved flare spectra by the  $2T_{\text{apex}}$  models (left: 190917; right: 191210). The red/blue color shows the cool/hot plasma component. In the  $kT$  plots, the solid lines and filled areas are the best-fit  $kT$  linear models and 90% confidence areas. In the EM plots, the data points show the best-fit values and 90% confidence ranges of the combined spectral fits. The solid lines show the best-fit linear rise plus exponential decay model to these EM measurements. In each flare, the cool component rises similarly to the hot component but with a time delay.

**Table 2**  
Flare Parameters

Flare	Comp.	$kT(t=0)$ (keV)	$kT_{\text{slope}}$ (keV $\text{ks}^{-1}$ )	$t_{\text{onset}}$ (s)	$\Delta t_{\text{rise}}$ (s)	$\tau_{\text{decay}}$ (s)	$\text{EM}_{\text{peak}}$ ( $10^{52} \text{ cm}^{-3}$ )	$L_{\text{Xpeak}}$ ( $10^{29} \text{ erg s}^{-1}$ )	$E_{\text{X}}$ ( $10^{32} \text{ erg}$ )	$E_{\text{bol}}$ ( $10^{33} \text{ erg}$ )
190917	Cool	$1.00^{+0.11}_{-0.13}$	$-0.18^{+0.25}_{-0.24}$	156 (20)	218 (fix)	572 (fix)	0.71 (0.061)	1.2	0.79	2.0/3.2
	Hot	$2.86^{+0.51}_{-0.46}$	$-1.6^{+0.96}_{-0.95}$	14 (7)	218 (15)	572 (86)	2.6 (0.13)	3.2	2.2	
191210	Cool	$1.02^{+0.03}_{-0.04}$	$-0.13^{+0.02}_{-0.01}$	227 (35)	923 (99)	2591 (324)	0.45 (0.032)	0.75	2.3	6.6/4.0
	Hot	$3.65^{+0.24}_{-0.25}$	$-0.32^{+0.16}_{-0.09}$	33 (37)	1003 (59)	1135 (111)	2.8 (0.12)	3.9	6.4	

**Note.**  $kT(t=0)$ ,  $kT_{\text{slope}}$ : best-fit  $kT$  linear time variation model of the combined spectral fits. The errors show 90% confidence ranges.  $t_{\text{onset}}$ ,  $\Delta t_{\text{rise}}$ ,  $\tau_{\text{decay}}$ ,  $\text{EM}_{\text{peak}}$ : best-fit linear rise plus exponential decay model of the EM time series. The parentheses show  $1\sigma$  confidence ranges.  $L_{\text{Xpeak}}$ : peak X-ray luminosity between 0.3 and 10 keV.  $E_{\text{X}}$ : total X-ray flare energy between 0.3 and 10 keV.  $E_{\text{bol}}$ : total bolometric flare energy. The left values use a relation to the GOES band (1.55–12.4 keV) flare-radiated energy for active stars (Table 2 in Osten & Wolk 2015). The right values use a relation to the GOES band solar flare peak flux (Equation (13) in Aschwanden et al. 2017).

10 (Del Zanna et al. 2021). We use the elemental abundances derived from the XMM/RGS spectra (Table A1), but our preliminary study using solar elemental abundances provides a similar result. Our simulations assume a magnetic loop with a uniform cross section and injected particles with a power-law energy distribution for 200 s with an energy flux peaking at  $10^{11.5} \text{ erg cm}^{-2} \text{ s}^{-1}$  at 100 s. Since the two NICER flares have different flare decay timescales and plausibly different magnetic loop lengths (e.g., Reep & Toriumi 2017; Toriumi et al. 2017), the simulations consider loop lengths at 5, 10, 15, 20, and  $25 \times 10^9 \text{ cm}$ . The derived EM normalization can be adjusted by changing the cross section of the magnetic loops (equivalently, the total volume of the loops).

The left panel of Figure 7 shows the EM evolution of the  $10 \times 10^9 \text{ cm}$  flare loop simulation. The EM is dominated by the hottest plasma emission that peaks near  $\sim 600 \text{ s}$ . This component represents a radiative cooling, evaporated plasma that fills the magnetic loop, corresponding to the hot component of the observing flares. Since the evaporated plasma cools down gradually under thermal equilibrium, a single temperature bucket dominates near its peak and drops to zero quickly once the plasma cools. A secondary component is a group of low-temperature buckets that rises and falls similarly to the main component at one-third the EM of the evaporated plasma

component. Each temperature bucket stays in this group until the evaporated plasma cools down to its temperature range. This secondary component represents plasmas at transition regions near the magnetic footpoints. Because the conductive heat flows from the loop top to the footpoints, the plasma has a strong temperature gradient and responds to the evaporated plasma's variation. The other loop length simulations show similar EM variations with different time scales.

In the first 500 s, the  $\log T \geq 7.3 \text{ K}$  buckets only reflect the evaporated plasma component, while the  $\log T < 7.0 \text{ K}$  buckets reflect the footpoint plasma component. We therefore define two temperature ranges,  $\log T = 7.3\text{--}8.0$  and  $6.6\text{--}6.9 \text{ K}$ , and sum up EMs within each range to understand their behaviors near the rising phase (Figure 7, right). First, the EM[6.6–6.9] time series of various loop lengths vary similarly for  $\sim 200 \text{ s}$  from the beginning. This EM base originates from the initial heating of the plasma in the upper chromosphere by the injected particles and peaks at  $\sim 100 \text{ s}$  in response to the assumed particle injection flux. The EM[7.3–8.0] does not show this component clearly, but the slow rise in the first  $\sim 50 \text{ s}$  originates from the initial plasma heating.

All EM[6.6–6.9] plots except the  $5 \times 10^9 \text{ cm}$  simulation show the footpoint components' onsets as clear kinks (e.g., at  $\sim 150 \text{ s}$  for the  $10 \times 10^9 \text{ cm}$  simulation). We measure the

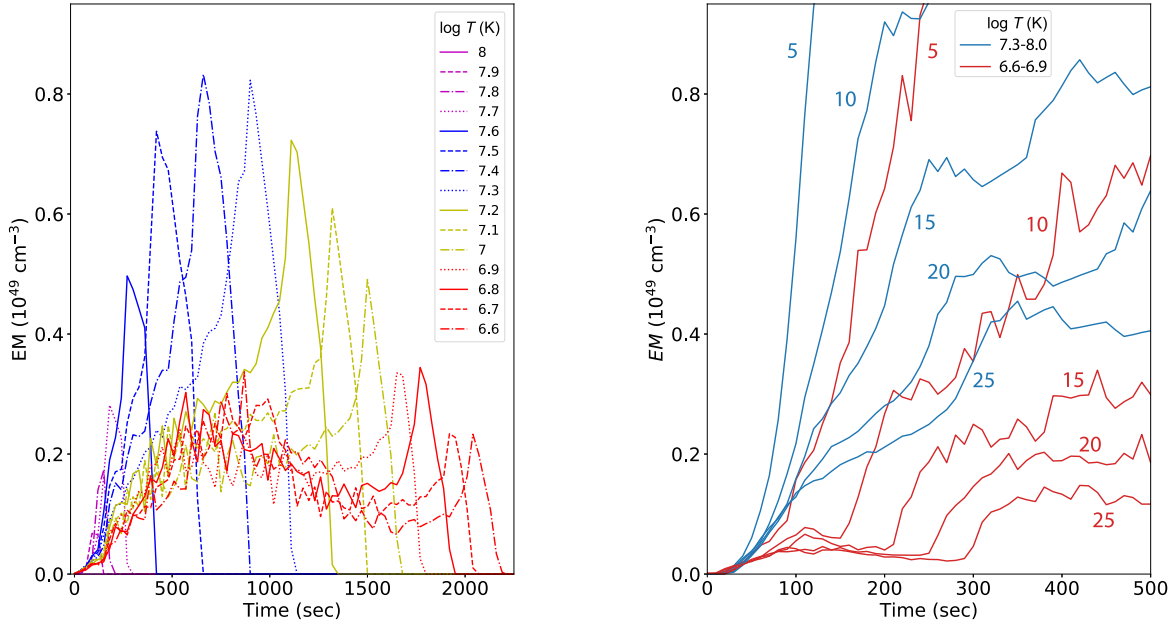


**Figure 7.** Left: whole loop EM variations of the  $10 \times 10^9$  cm loop simulation. The EMs are divided by logarithmic temperature buckets and binned every 30 s. The plot shows two EM components: the evaporated plasma that envelopes individual temperature peaks standing up from the hot side, getting a maximum at  $\sim 600$  s, and the footpoint plasma, a group of low-temperature buckets that rises and falls similarly at one-third of the evaporated plasma component. Right: whole loop EM variations for the first 500 s, summed over the temperature ranges  $\log T = 7.3\text{--}8.0$  (blue) and  $6.6\text{--}6.9$  K (red). The number that labels each line is the loop length in  $10^9$  cm. The evaporated component starts to rise at  $\sim 50$  s, while the footpoint component is significantly delayed from the evaporated component, and more with longer loops. The overlapping triangular base in the red plot up to  $\sim 250$  s originates from the initial heating.

**Table 3**  
HYDRAD Simulation Result

Loop Length ( $10^9$ cm)	$t_{\text{onset}}(\text{eva})$ (s)	$t_{\text{onset}}(\text{foot})$ (s)	$\Delta t_{\text{delay}}$ (s)	$\Delta t_{\text{rise}}(\text{eva})$ (s)	$\tau_{\text{decay}}(\text{eva})$ (s)	EM <sub>peak</sub> Ratio	$kT_{\text{peak}}(\text{Cool/Hot})$ (keV/keV)
5	63	77	15	330	760	1.21	0.32/1.40
10	64	153	89	491	1207	1.04	0.31/1.67
15	40	205	164	496	2268	0.78	0.32/1.66
20	25	248	223	639	3013	0.65	0.34/1.57
25	17	294	276	752	3601	0.60	0.35/1.57
Flare190917			142	218	572	0.27	0.96/2.50
Flare191210			194	1003	1135	0.16	0.88/3.31

**Note.** In each simulation, the time origin is the particle injection start.  $t_{\text{onset}}(\text{eva})/t_{\text{onset}}(\text{foot})$ : onset time of the evaporated/footpoint component derived from one/two linear fits to the EM[7.3–8.0]/EM[6.6–6.9] time series.  $\Delta t_{\text{delay}} = t_{\text{onset}}(\text{foot}) - t_{\text{onset}}(\text{eva})$ .  $\Delta t_{\text{rise}}(\text{eva})/\tau_{\text{decay}}(\text{eva})$ : rise/decay time of the evaporated component derived from a fit to the peak EMs of individual temperature buckets by a linear rise plus exponential decay model. EM<sub>peak</sub> ratio,  $kT_{\text{peak}}(\text{cool/hot})$ : EM<sub>peak</sub> ratio and plasma temperatures at the cool/hot EM peaks, derived from fits to the synthetic flare spectra with 100 s bins by a  $2T_{\text{apex}}$  model.

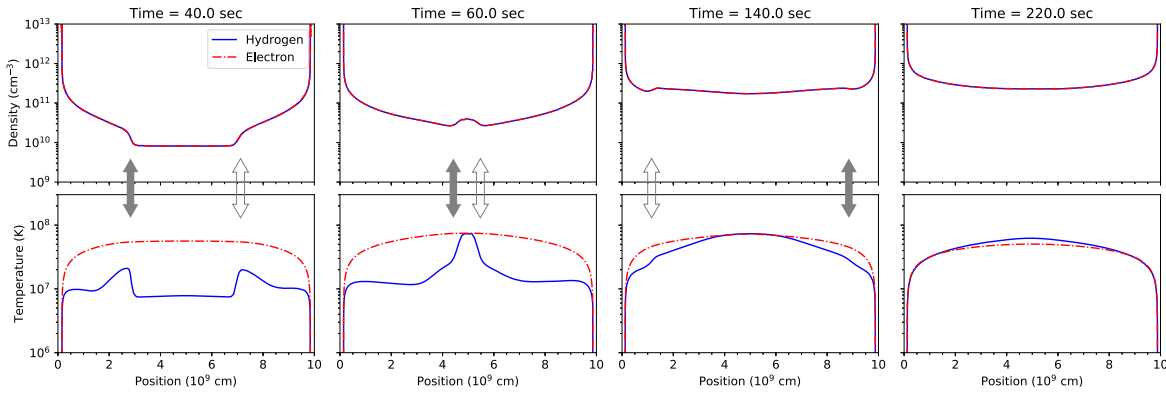
timing of each kink from a fit with a continuous piecewise linear function ( $t_{\text{onset}}(\text{foot})$  in Table 3). The onset ranges between  $\sim 80$  and 300 s, and longer loops have later onsets. The evaporated component does not have a clear onset signature, so we measure the onset timing from a fit to the first 200 s of EM [7.3–8.0] by a linear function starting at  $t_{\text{onset}}(\text{eva})$ . The onset ranges between 17 and 64 s and does not appear to correlate with the loop length. The time lags  $\Delta t_{\text{delay}} (=t_{\text{onset}}(\text{foot}) - t_{\text{onset}}(\text{eva}))$  clearly increase with longer loops.

Figure 8 shows why the footpoint component is delayed. In the plots, the evaporated component is located in the middle part, where temperature and density quickly increase after the particle injection. The footpoint component is located near both ends, whose temperature and density do not increase until the shocks produced by the evaporated gas’s collision at the loop top propagate down to the footpoints. Figure 9 displays the hydrogen and electron density product and the electron temperature, magnifying the left end on a logarithmic scale.

Both the  $\log T = 6.6\text{--}6.9$  K depth and density product increase between 140 and 220 s. The time delay corresponds to the travel time of the flare loop by the evaporated flows and the collisional shocks, which is approximately the sound-crossing time. It is, therefore, roughly proportional to the loop length.

We also measure the decay timescales of the simulated flares. As described above, the evaporated plasma is in a single temperature bucket at each temperature peak. We thus take the peak EM of each temperature bucket and fit them by a linear plus exponential decay model from Equation (1). The fits reproduce the EM variations well, except around the peak (Figure 10 for the  $10 \times 10^9$  cm loop simulation). Longer loop flares have longer decay timescales ( $\tau_{\text{decay}}(\text{eva})$  in Table 3), as suggested in earlier studies (e.g., van den Oord & Mewe 1989; Toriumi et al. 2017).

We make synthetic NICER spectra of the simulated EM distributions to compare the spectral properties. For each simulation, we produce spectral models with 100 s bins,



**Figure 8.** Density (top) and temperature (bottom) spatial distribution of the  $10 \times 10^9$  cm loop simulation at 40, 60, 140, and 220 s from the particle injection start. The horizontal axis shows the distance from a footpoint along the loop; the loop top is at  $5 \times 10^9$  cm, and the two footpoints are at 0 and  $10 \times 10^9$  cm. From left, (i) at 40 s, the particle injection heats the footpoint chromosphere, and the evaporated gas soars into the magnetic loop. The evaporated spectral component starts to increase. (ii) At 60 s, the upward evaporation flows collide at the loop top, heating the gas further. (iii) At 140 s, the shock propagates down the other leg, smoothing the corona’s density. (iv) At 220 s, by the time the shock reaches the footpoints, the loop has enough high density that thermal conduction becomes extremely efficient, and the footpoint spectral component emerges. The red and blue lines are for electrons and hydrogen, respectively. The black and white double arrows point to the locations of the evaporation or shock fronts from either side.

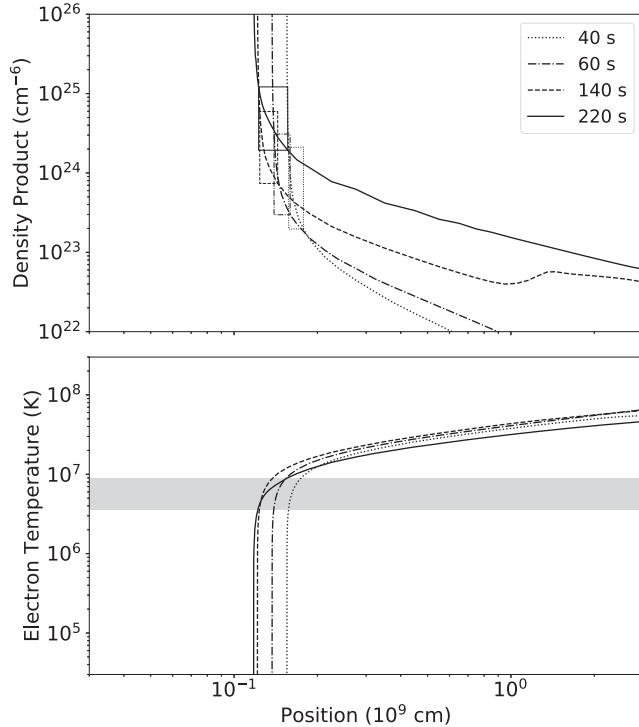


**Figure 9.** Electron and hydrogen density product (top) and electron temperature (bottom) distributions of the  $10 \times 10^9$  cm loop simulation near a footpoint region at  $t = 40$  (dotted), 60 (dashed-dotted), 140 (dashed), and 220 (solid) s. The horizontal axis is the same as Figure 8 but on a logarithmic scale. The filled gray area in the bottom panel shows the  $\log T = 6.6\text{--}6.9$  K bucket. The boxes in the top panel show the one-dimensional volumes and density product ranges of this temperature bucket. Both the density product and the volume significantly increase between  $t = 140$  and 220 s.

assuming an *apec* plasma model for each temperature bucket. We normalize them to a peak 0.3–2 keV flux at  $2.2 \times 10^{-11} \text{ erg cm}^{-2} \text{ s}^{-1}$  to match the two observed NICER flares. We then generate a synthetic spectrum for each spectral model with the *xspec fakeit* tool by convolving the model with the NICER on-axis responses, *nixtref20170601v003.rmf* and *nixtiaveonaxis20170601v005.arf*. We increase the photon statistics by a factor of 10 to reduce statistical uncertainty, equivalent to a 1 ks exposure. We then bin each synthesized

spectrum to have  $\geq 50$  counts  $\text{bin}^{-1}$  and fit each spectrum by a *2T\_apec* model. Figure 11 (left) shows a synthetic spectrum of the  $10 \times 10^9$  cm loop between 600 and 700 s, adding the quiescent component of the September flare for comparison. Table 3 shows the  $\text{EM}_{\text{peak}}$  ratios and plasma temperatures at the EM peaks. The peak plasma temperatures,  $\sim 0.3\text{--}0.35$  and  $1.4\text{--}1.67$  keV, are similar among the simulations and significantly lower than the observed values. The  $\text{EM}_{\text{peak}}$  ratio is the highest with the  $5 \times 10^9$  cm loop simulation at 1.21 and smaller with longer loop simulations. This result is naturally understood, since the footpoint plasma volume does not change with the loop length.

The numerical simulations demonstrate that the footpoint component rise is delayed by 100–300 s from the evaporated component. This result indicates that the cool component in the NICER spectra originates from the footpoint plasma. The simulations also suggest that longer flare loops have longer delays of the footpoint component rise and smaller EM peak ratios, as well as longer decay timescales. All of these properties are consistent with the properties of the two NICER flares, suggesting that the December flare originates from a longer flare loop than the September flare.

## 5. Discussion

The  $\kappa^1$  Ceti flares in 2019 are more powerful than the most powerful solar flare ever seen, the Carrington Event in 1859 ( $L_X \sim 10^{28} \text{ erg s}^{-1}$ ; Cliver & Dietrich 2013; Sakurai 2022). Their X-ray luminosities are near the upper end of the flare luminosity ranges of solar-type G stars ( $L_X \lesssim 10^{30} \text{ erg s}^{-1}$ ; Schaefer et al. 2000; Tsuboi et al. 2016). Their bolometric flare-radiated energies of  $3\text{--}8 \times 10^{33} \text{ erg}$ , evaluated from two independent empirical relations to the X-ray radiation among solar and active stellar flares (Osten & Wolk 2015; Aschwanden et al. 2017; see Table 2), qualify them as superflares ( $> 10^{33} \text{ erg}$ ; e.g., Maehara et al. 2012) and are comparable to the  $\kappa^1$  Ceti superflare recorded in 1986 ( $\sim 2 \times 10^{34} \text{ erg}$ ; Schaefer et al. 2000). Nonetheless, their X-ray luminosities and released X-ray energies are modest among active or young stellar flares ( $L_X \lesssim 10^{32\text{--}33} \text{ erg s}^{-1}$ ; e.g., Benz & Güdel 2010, and references therein). The other X-ray characteristics—the hot plasma temperature, hard-band light curve, and hardness

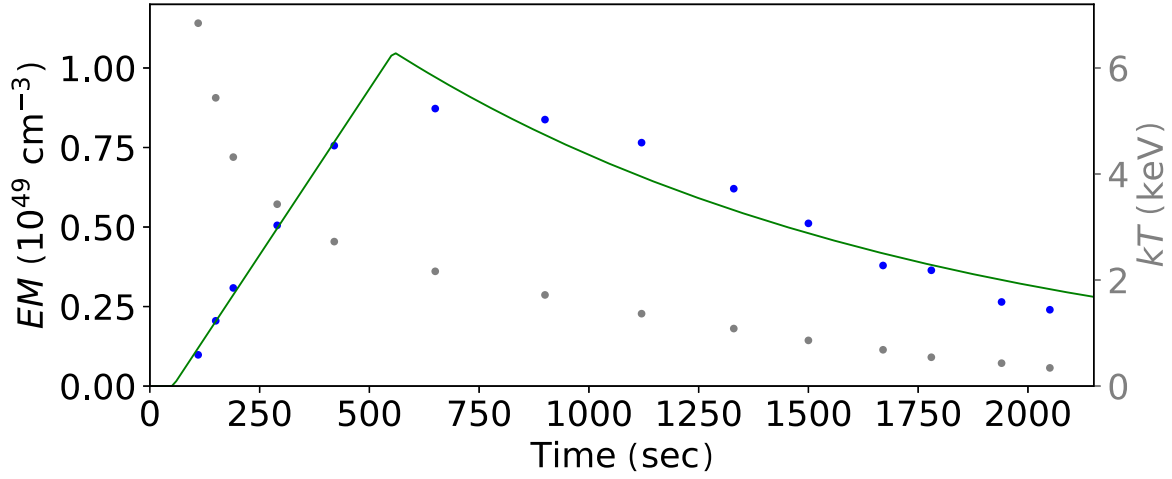


**Figure 10.** The EM value (blue) at each temperature bucket peak and the corresponding plasma temperature (gray) in the  $10 \times 10^9$  cm loop simulation. The solid green line is the best-fit model of the EM values by a linear plus exponential decay model. The model reproduces the EM variation well.

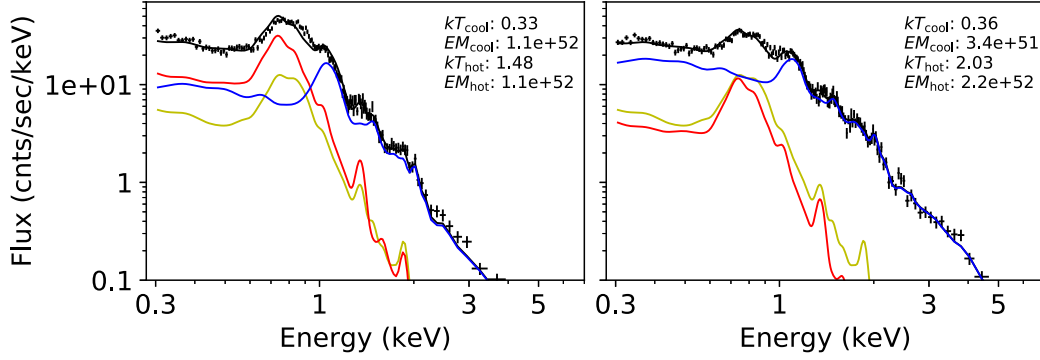


**Figure 11.** Left: synthetic NICER spectrum of the  $10 \times 10^9$  cm simulation at the flare peak (600–700 s). The flare spectrum is normalized to have the 0.3–2 keV flux at  $2.2 \times 10^{-11}$  erg cm $^{-2}$  s $^{-1}$  and combined with the quiescent spectrum of the September flare. Right: same spectrum but with EMs below the evaporated plasma temperature ( $\log T < 7.3$ ) reduced to 10%. The left spectrum has strong emission at  $\sim 0.8$  keV, while the right spectrum is close to the observed flare peak spectra. The upper right corner of each panel shows the best-fit parameters of a  $2T$  apec model (the units are keV for  $kT$  and cm $^{-3}$  for EM). Each plot uses the same color scheme as in Figures 4 and 5.

ratio variation—are similar to solar and stellar X-ray flares (e.g., Pye et al. 2015). We conclude that the  $\kappa^1$  Ceti flares in 2019 are conventional magnetic reconnection events.

The  $\kappa^1$  Ceti flare spectra require an additional cool ( $kT \lesssim 1$  keV) temperature component. Although such a component has not received much attention, well-exposed stellar X-ray flare spectra usually require one or more components with  $kT \sim 0.3$ –1 keV (e.g., GT Mus, Sasaki et al. 2021; EV Lac, Paudel et al. 2021). The high-resolution XMM/RGS spectra of the Proxima Centauri flare suggested that the flare EM distribution was broad with a peak at  $\sim 30$  MK and a low-temperature tail during the rise and steadily moved to low temperatures as the flare developed (Güdel et al. 2004; Reale et al. 2004). In solar flares, the low-temperature EM ( $< 16.5$  MK) peaks later than the high-temperature EM (McTiernan et al. 1999), perhaps suggesting the presence of a similar cool component. The cool component is probably ubiquitous in solar and stellar flares and represents an average of the low-temperature tail in the EM distribution.

The cool component’s EMs of the  $\kappa^1$  Ceti flares increase steadily during the rising phase, but the footpoint plasma’s EMs in the HYDRAD simulations rapidly increase to half the maximum at the onsets. The September flare may be statistics-limited due to its quick rise, but the December flare clearly

shows that the cool component’s EM steadily increases with a possible stepwise increase in the middle of the rise. This may suggest that each flare is an assembly of multiple loops, which is well known from, e.g., spatially resolved UV and optical imaging of solar flares (e.g., Aschwanden & Alexander 2001). Multiple loop models can reproduce energy-dependent X-ray time variations of solar flares (Reep & Toriumi 2017).

If the observed flares are multiple loop events, we should ideally convolve the HYDRAD simulations with single loop event rates. Very hard X-rays ( $> 20$  keV) or microwave emission can trace the flux variation of the injected nonthermal reconnection particles (e.g., Benz 2017), but we do not have simultaneous data in these bands, unfortunately. Earlier flare observations suggest that these emissions drop before the soft X-ray peaks (Lin et al. 2003; Asai et al. 2004; Veronig et al. 2005), which are  $\sim 200$  s in the September flare and  $\sim 1$  ks in the December flare. A convolution in each timescale may change the EM<sub>peak</sub> ratio and flare decay timescale. It should not change the cool-component delay timescales.

We compare the derived  $\kappa^1$  Ceti flare parameters,  $\Delta t_{\text{delay}}$ ,  $\tau_{\text{decay}}$ , and the EM<sub>peak</sub> ratio with the simulation (Table 3). These values vary monotonically with the loop length in the simulation, so we estimate the loop length for each parameter by linearly interpolating or extrapolating the two neighboring



**Table 4**  
Flare Loop Length Estimate

Flare	HYDRAD			Sun	QS	SY02
	$\Delta t_{\text{delay}}$	EM <sub>peak</sub>	Ratio			
190917	13.5	60.3	2.9	6.2	8.9	12.9
191210	17.6	72.3	9.2	13.6	22.5	8.7

**Note.** Units in  $10^9$  cm. HYDRAD: linear interpolation or extrapolation of the nearest two values of the HYDRAD simulation in Table 3. Sun: solar flare ribbon distance relation in Equation (4) of Toriumi et al. (2017). The derived  $d_{\text{ribbon}}$  values are multiplied by  $\pi/2$ . QS: quasi-static cooling model in Tsuboi et al. (2000), Equation (A5). SY02: Equation (7b) in SY02 for the preflare proton density at  $10^{11} \text{ cm}^{-3}$ .

values (Table 4). We also list three other estimates from the literature. The first estimate is an empirical relation of the ribbon distance with the decay timescale in solar flares (Toriumi et al. 2017, Equation (4)). We approximate the decay timescale of the 1–8 Å energy flux with  $\tau_{\text{decay}}$  of the hot component in Table 2 and assume a semicircular flare loop shape to derive the loop length. The second estimate is a quasi-static cooling model for a constant radiative and conductive timescale ratio (van den Oord & Mewe 1989; Tsuboi et al. 2000, Equation (A5)). A problem with this estimate is that flares never truly cool statically (e.g., Cargill et al. 1995). The third estimate is a magnetic reconnection model, assuming that the gas pressure of a flare loop is comparable to the magnetic pressure (Shibata & Yokoyama 2002, hereafter SY02). A caveat is that the model requires the unmeasurable preflare proton density. All estimates but the EM<sub>peak</sub> ratio are consistent with  $\approx 10^{10}$  cm loop lengths. All estimates but SY02 suggest that the December flare has a longer flare loop than the September flare.

The derived loop length of  $\approx 10^{10}$  cm is near the upper end but still within the range of solar flare loops (e.g., Toriumi et al. 2017). Since  $\kappa^1$  Ceti has about the same stellar radius as the Sun, we can safely assume that the observed  $\kappa^1$  Ceti flares have similar magnetic field geometries to moderately large solar flare loops. However, the peak EMs,  $\sim 3 \times 10^{52} \text{ cm}^{-3}$ , are about 2 orders of magnitude larger than the EMs of solar flares with similar loop lengths. One solution is that the  $\kappa^1$  Ceti flares have an order-of-magnitude higher flare plasma density. Such high-density plasma radiatively cools with order-of-magnitude shorter timescales, but  $\kappa^1$  Ceti’s flare decay timescales are consistent with the solar flare’s decay time relation (Table 4). The other solution is that  $\kappa^1$  Ceti flares have 2 orders of magnitude larger widths and/or thicker magnetic loops.

The EM<sub>peak</sub> ratio derives inconsistent loop lengths, possibly because the HYDRAD simulation systematically overestimates the footpoint component. The footpoint component is comprised of all temperature buckets below the evaporated plasma temperature (see Figure 7, left). We therefore reduce the footpoint component’s EMs of the simulation shown in Figure 11 (left) simulation—the EMs below the evaporated plasma temperature,  $\log T = 7.3$  (K)—to 10% as a trial. Then, the synthetic spectrum looks more similar to the observed spectra near the flare peaks (Figure 11, right), and the best-fit 2T apec model has a smaller EM<sub>peak</sub> ratio at  $\sim 0.18$ . As observed, this model also derives a higher hot-component temperature at 2.0 keV.

The footpoint plasma at the height of  $\sim 1.2\text{--}1.6 \times 10^8$  cm is in the transition region (Figures 8 and 9). The line of sight

should have more intervening material than the evaporated plasma in the corona. Still, attenuating  $\sim 0.9$  keV X-rays by  $\sim 80\%$  requires a hydrogen column density at  $N_{\text{H}} \sim 10^{22} \text{ cm}^{-2}$ , corresponding to a physical depth of  $\sim 10^{10\text{--}11}$  cm for the density of the transition region ( $n \sim 10^{11\text{--}12} \text{ cm}^{-3}$ ). Flare loops need to be viewed almost edge-on to have this depth, but realizing such geometries for both loops is less likely. Therefore, the observed flares should have less footpoint plasma to the evaporated plasma than the HYDRAD simulations. The RHESSI observatory found in the hard X-ray band ( $>10$  keV) that solar flares have several times higher electron rates at the loop top than at the footpoints during the impulsive phase,<sup>10</sup> implying that the electrons accumulate in the loop top (Simões & Kontar 2013). The  $\kappa^1$  Ceti flares may also have a mechanism to suppress electron transportation to the footpoints and reduce thermal conduction. Such a mechanism may also explain the slower cooling of the evaporated plasma compared to the HYDRAD simulations.

One possible mechanism to suppress electron transport is that the flare magnetic loop expands toward the loop top, trapping charged particles in a magnetic mirror. Solar coronal loops, whether quiescent or flaring, do not necessarily show an expansion of the loop width along their lengths (Klimchuk et al. 1992; Klimchuk 2000; Klimchuk & DeForest 2020, and references therein). However, the magnetic field strength falls off with height in the corona, implying that there should be an expansion of the cross-sectional area of the loops (e.g., Dudík et al. 2014), and models are unable to reproduce both hot and cool emission simultaneously without an area expansion (Warren et al. 2010; Reep et al. 2022). The loop expansion reduces the thermal conductivity near the footpoints. A preliminary  $10 \times 10^9$  cm loop simulation with the expansion geometry in Reep et al. (2022b) does not produce a small EM<sub>peak</sub> ratio, but the cool-component EM peaks significantly later than the constant loop simulation. The other possible mechanism is that the flare loops have turbulent magnetic fluctuations, which would increase the frequency of Coulomb collisions, suppressing the energy transport and reducing the thermal conductivity (e.g., Bian et al. 2016; Allred et al. 2022). This mechanism increases coronal temperatures compared to those in a model with collisionally dominated transport.

## 6. Conclusion

NICER observed two moderately strong X-ray flares from  $\kappa^1$  Ceti, a nearby young solar analog, in 2019. NICER’s excellent soft X-ray sensitivity, good energy resolution, and large collecting area bring rare details of bright X-ray flares from the onsets through the peaks. Both flares show conventional stellar flare variations above 2 keV with a rapid rise and decay, having similar X-ray fluxes at  $\sim 2.2 \times 10^{-11} \text{ erg cm}^{-2} \text{ s}^{-1}$  between 0.3 and 2 keV and high plasma temperatures at  $\sim 3$  keV near the peaks. Their bolometric energies estimated from the X-ray radiated energies,  $\sim 3\text{--}9 \times 10^{32} \text{ erg}$ , are comparable to superflares. The flare on September 17 varies in several hundred seconds in X-rays, with an interesting flat soft X-ray flux peak. The flare on December 10 varies two to four times more slowly, showing a similar but less extreme variation in the soft band.

<sup>10</sup> During the impulsive phase, the magnetic reconnection accelerates charged particles, which emit hard nonthermal X-rays (e.g., Benz 2017). This phase occurs mostly before the cool component rises.



The time-resolved spectra show that, in the rising phase, the hard-band slope increases first, and a hump at  $\sim 0.9$  keV, originating from the Fe L line complex, follows. Most spectra require two optically thin thermal plasma temperature components at  $kT \sim 1$  and  $\sim 3$  keV on top of the quiescent component. The hot component mainly reproduces the hard-band slope, and the cool component does the 0.9 keV hump. Both components' EMs rise linearly on similar timescales, but the cool component is delayed by 100–200 s. The September flare has a longer delay time relative to the flare rise duration and a more substantial cool component than the December flare, producing a heavily rounded flare peak.

The HYDRAD field-aligned numerical simulations demonstrate that the cooler footpoint plasmas start to increase a few hundred seconds after the hot evaporated plasmas increase; longer flare loops have longer time delays and weaker cool components. This result indicates that the cool components in the  $\kappa^1$  Ceti flares originate primarily from the footpoint plasma and that the September flare stems from a shorter flare loop than the December flare. The estimated loop lengths of  $\approx 10^{10}$  cm are large but still within the range of the solar flare loops. Since the  $\kappa^1$  Ceti flares have more than 2 orders of magnitude larger EMs than the solar flares, they need significantly higher loop plasma densities or thicknesses. A significant discrepancy in the  $EM_{\text{peak}}$  ratio may suggest that the HYDRAD simulations overestimate the footpoint EMs and require a mechanism to suppress electron transport, such as expanded magnetic loops or turbulent magnetic fluctuations. A difference in the cool component's EM rise may suggest that both flares are multiple loop events, as seen in solar flares.

NICER's  $\kappa^1$  Ceti observations and the HYDRAD simulations demonstrate that the time delay of the cool component and the peak EM ratio of the two temperature plasma components can be used as new, effective parameters for estimating the flare loop length. We should confirm the derived relations with more flare samples of various luminosities, durations, peak temperatures, and stellar types with existing or future NICER observations. Simultaneous multiwavelength observations will also greatly help constrain the flare parameters. In particular, UV and optical observations with the Hubble Space Telescope or the TESS observatory trace hot chromospheric gas, helping to understand the whole chromospheric and coronal heating process. The HYDRAD numerical simulations still have discrepancies with the observations. We should decipher the cause with further studies and improve the model to explain the observations.

This material is based upon work supported by NASA under award No. 80GSFC21M0002. J.W.R. was supported by the Office of Naval Research 6.1 Support Program. V.S.A. acknowledges the funds from NICER GO Cycle 2 project award No. 80NSSC21K0101. This work is supported by JSPS KAKENHI grant Nos. JP20KK0072, JP21H01124, and JP21H04492 and NINS grant Nos. 01321802 and 01311904. This research has made use of data and/or software provided by the High Energy Astrophysics Science Archive Research Center (HEASARC), which is a service of the Astrophysics Science Division at NASA/GSFC. We thank Mr. Craig Gordon for helping resolve a PYXSPEC problem. We thank Dr. Andrew Pollock for suggestions of XMM-Newton RGS data analysis. We thank Drs. Stephen Drake, Ryo Sasaki, Yuta

Notsu, Michael F. Corcoran, and Konstantin V. Getman for discussions about stellar flare physics.

*Facilities:* NICER(XTI), XMM(RGS).

*Software:* HEASoft (Nasa High Energy Astrophysics Science Archive Research Center (Heasarc), 2014), xspec (Arnaud 1996), scipy (Virtanen et al. 2020), astropy (Astropy Collaboration et al. 2013; Scargle et al. 2013), SAS (v19.0; Gabriel et al. 2004), HYDRAD (Bradshaw & Mason 2003).

## Appendix Elemental Abundance Measurement

Telleschi et al. (2005) extensively studied the coronal elemental abundance of  $\kappa^1$  Ceti using XMM/RGS data in 2002. However, the XMM-Newton instrumental calibration<sup>11</sup> and the plasma emission codes (e.g., ATOMDB<sup>12</sup>) have significantly improved since then. The elemental abundance of the star might also have changed in 17 yr. We thus independently measure the coronal elemental abundance of  $\kappa^1$  Ceti using the XMM/RGS data obtained on 2018 July 30 and 2019 January 29 (ObsIDs: 0822790901, 0822791001; PI: Wargelin).

We reprocess these data sets with SAS version 19.0.<sup>13</sup> EPIC/MOS2 turns off during these observations, while EPIC-pn uses the timing mode with relatively poor spectral resolution. We thus analyze EPIC/MOS1 and RGS data. For MOS1, we take a  $15''$  radius circular source region centered at the X-ray peak position. The MOS1 on-axis CCD operates with the small window mode so that we take background data from a source-free region from the surrounding CCDs. The MOS1 light curves of these observations do not show significant time variations. EPIC/MOS1 measures the 0.6–1.2 keV flux during the second observation at  $\sim 3.5 \times 10^{-12}$  erg cm<sup>-2</sup> s<sup>-1</sup>, which is  $\sim 16\%$  lower than the first observation. This flux is nearly the lowest among the NICER monitoring observations of  $\kappa^1$  Ceti.

We produce the MOS1 spectra using the same source and background regions. For RGS, we run `rgsproc` for the target position measured from the MOS1 image and produce the source and background spectra (Figure A1). We only use the first-order RGS spectra, as the second-order RGS spectra do not have enough photon counts to identify emission lines. We fit the unbinned MOS1 and RGS spectra simultaneously using the Cash statistic (`c-stat`) built in `xspec` (Cash 1979). The Cash statistic needs to add background as an additive model component so that we simultaneously fit background spectra by an empirical model (`power-law + 4 Gaussians`), convolved with the source response (`rmf`) weighted with the background areal scale (`backscal`). For the source spectra, we assume a  $2T$  thermal plasma model with various abundance values (`vappec`) and fit all MOS1/RGS source/background spectra of the two observations simultaneously. We allow for varying spectral normalization between MOS1 and RGS to account for calibration uncertainty and  $kT$  and normalization between the two observations for time variation. Table A1 lists the derived elemental abundance. We use these values for the NICER data analysis and numerical simulation.

<sup>11</sup> <https://www.cosmos.esa.int/web/xmm-newton/calibration-documentation>

<sup>12</sup> <http://www.atomdb.org>

<sup>13</sup> <https://www.cosmos.esa.int/web/xmm-newton/sas>

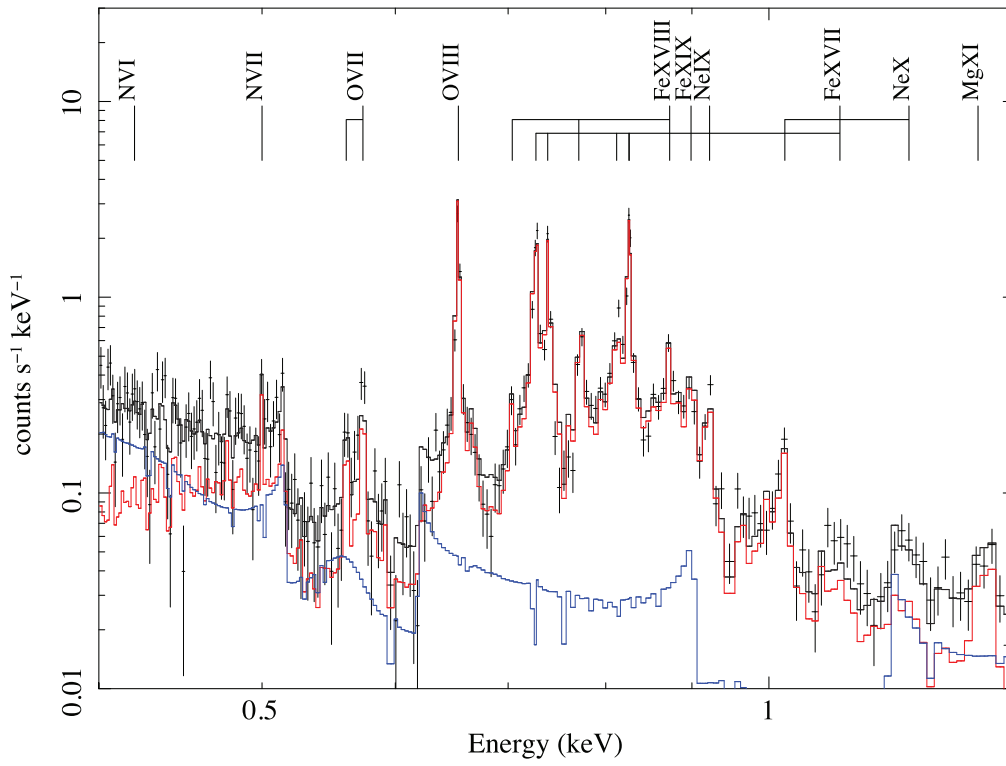


**Figure A1.** The XMM-Newton RGS1 + 2 grating spectrum of  $\kappa^1$  Ceti combined from the 2018 and 2019 observations. The spectrum includes both source and background data (black). The red line shows the best-fit  $2T$  *apec* model, and the blue line shows the corresponding background model. The black line is the sum of these models. The prominent emission lines are labeled.

**Table A1**  
Applied Elemental Abundance

Element	$\kappa^1$ Ceti		Sun Number
	Relative to Sun	Number	
H	1.00 <sup>f</sup>	1.00E+00	1.00E+00
He	1.00 <sup>f</sup>	8.51E-02	8.51E-02
Li	1.00 <sup>f</sup>	1.12E-11	1.12E-11
Be	1.00 <sup>f</sup>	2.40E-11	2.40E-11
B	1.00 <sup>f</sup>	5.01E-10	5.01E-10
C	0.42	1.12E-04	2.69E-04
N	0.44	2.99E-05	6.76E-05
O	0.40	1.95E-04	4.90E-04
F	1.00 <sup>f</sup>	3.63E-08	3.63E-08
Ne	0.62	5.29E-05	8.51E-05
Na	1.00 <sup>f</sup>	1.74E-06	1.74E-06
Mg	0.68	2.70E-05	3.98E-05
Al	1.00 <sup>f</sup>	2.82E-06	2.82E-06
Si	0.55	1.77E-05	3.24E-05
P	1.00 <sup>f</sup>	2.57E-07	2.57E-07
S	0.19	2.51E-06	1.32E-05
Cl	1.00 <sup>f</sup>	3.16E-07	3.16E-07
Ar	0.19	4.83E-07	2.51E-06
K	1.00 <sup>f</sup>	1.07E-07	1.07E-07
Ca	0.58	1.28E-06	2.19E-06
Sc	1.00 <sup>f</sup>	1.41E-09	1.41E-09
Ti	1.00 <sup>f</sup>	8.91E-08	8.91E-08
V	1.00 <sup>f</sup>	8.51E-09	8.51E-09
Cr	1.00 <sup>f</sup>	4.37E-07	4.37E-07
Mn	1.00 <sup>f</sup>	2.69E-07	2.69E-07
Fe	0.64	2.03E-05	3.16E-05
Co	1.00 <sup>f</sup>	9.77E-08	9.77E-08
Ni	1.59	2.64E-06	1.66E-06
Cu	1.00 <sup>f</sup>	1.55E-08	1.55E-08
Zn	1.00 <sup>f</sup>	3.63E-08	3.63E-08

**Note.** Abundance numbers relative to H. Solar abundance reference: Asplund et al. (2009). <sup>f</sup>Fixed at the solar values in the XMM-Newton spectral fits.

## ORCID iDs

Kenji Hamaguchi  <https://orcid.org/0000-0001-7515-2779>  
 Jeffrey W. Reep  <https://orcid.org/0000-0003-4739-1152>  
 Vladimir Airapetian  <https://orcid.org/0000-0003-4452-0588>  
 Shin Toriumi  <https://orcid.org/0000-0002-1276-2403>  
 Keith C. Gendreau  <https://orcid.org/0000-0001-7115-2819>

## References

Airapetian, V. S., Barnes, R., Cohen, O., et al. 2020, *IJAsB*, **19**, 136  
 Airapetian, V. S., Jin, M., Lüftinger, T., et al. 2021, *ApJ*, **916**, 96  
 Allred, J. C., Kerr, G. S., & Gordon Emslie, A. 2022, *ApJ*, **931**, 60  
 Arnaud, K. A. 1996, in ASP Conf. Ser. 101, *Astronomical Data Analysis Software and Systems V*, ed. G. H. Jacoby & J. Barnes (San Francisco, CA: ASP), **17**  
 Asai, A., Yokoyama, T., Shimojo, M., & Shibata, K. 2004, *ApJL*, **605**, L77  
 Aschwanden, M. J., & Alexander, D. 2001, *SoPh*, **204**, 91  
 Aschwanden, M. J., Caspi, A., Cohen, C. M. S., et al. 2017, *ApJ*, **836**, 17  
 Asplund, M., Grevesse, N., Sauval, A. J., & Scott, P. 2009, *ARA&A*, **47**, 481  
 Audard, M., Güdel, M., & Mewe, R. 2001, *A&A*, **365**, L318  
 Astropy Collaboration, Robitaille, T. P., Tollerud, E. J., et al. 2013, *A&A*, **558**, A33  
 Benz, A. O. 2017, *LRSP*, **14**, 2  
 Benz, A. O., & Güdel, M. 2010, *ARA&A*, **48**, 241  
 Bian, N. H., Kontar, E. P., & Emslie, A. G. 2016, *ApJ*, **824**, 78

Bradshaw, S. J., & Cargill, P. J. 2013, *ApJ*, **770**, 12  
 Bradshaw, S. J., & Mason, H. E. 2003, *A&A*, **401**, 699  
 Cargill, P. J., Mariska, J. T., & Antiochos, S. K. 1995, *ApJ*, **439**, 1034  
 Cash, W. 1979, *ApJ*, **228**, 939  
 Cliver, Edward W., & Dietrich, William F. 2013, *JSWSC*, **3**, A31  
 Del Zanna, G., Dere, K. P., Young, P. R., & Landi, E. 2021, *ApJ*, **909**, 38  
 Dere, K. P., Landi, E., Mason, H. E., Monsignori Fossi, B. C., & Young, P. R. 1997, *A&AS*, **125**, 149  
 Dudík, J., Dzifčáková, E., & Cirtain, J. W. 2014, *ApJ*, **796**, 20  
 Emslie, A. G. 1978, *ApJ*, **224**, 241  
 Favata, F., Reale, F., Micela, G., et al. 2000, *A&A*, **353**, 987  
 Gabriel, C., Denby, M., Fyfe, D. J., et al. 2004, in ASP Conf. Ser. 314, *Astronomical Data Analysis Software and Systems (ADASS) XIII*, ed. F. Ochsenbein, M. G. Allen, & D. Egret (San Francisco, CA: ASP), **759**  
 Gendreau, K., & Arzoumanian, Z. 2017, *NatAs*, **1**, 895  
 Getman, K. V., Feigelson, E. D., & Garmire, G. P. 2021, *ApJ*, **920**, 154  
 Güdel, M., Audard, M., Reale, F., Skinner, S. L., & Linsky, J. L. 2004, *A&A*, **416**, 713  
 Güdel, M., Audard, M., Skinner, S. L., & Horvath, M. I. 2002, *ApJL*, **580**, L73  
 Güdel, M., & Nazé, Y. 2009, *A&ARv*, **17**, 309  
 Haisch, B., Strong, K. T., & Rodono, M. 1991, *ARA&A*, **29**, 275  
 Hawley, S. L., & Fisher, G. H. 1994, *ApJ*, **426**, 387  
 Klimchuk, J. A. 2000, *SoPh*, **193**, 53  
 Klimchuk, J. A., & DeForest, C. E. 2020, *ApJ*, **900**, 167  
 Klimchuk, J. A., Lemen, J. R., Feldman, U., Tsuneta, S., & Uchida, Y. 1992, *PASJ*, **44**, L181  
 Lin, R. P., Krucker, S., Hurford, G. J., et al. 2003, *ApJL*, **595**, L69  
 Lynch, B. J., Airapetian, V. S., DeVore, C. R., et al. 2019, *ApJ*, **880**, 97  
 Maehara, H., Shibayama, T., Notsu, S., et al. 2012, *Natur*, **485**, 478  
 McTiernan, J. M., Fisher, G. H., & Li, P. 1999, *ApJ*, **514**, 472  
 Mondal, B., Sarkar, A., Vadawale, S. V., et al. 2021, *ApJ*, **920**, 4  
 Nasa High Energy Astrophysics Science Archive Research Center (Heasarc) 2014, HEASoft: Unified Release of FTOOLS and XANADU, Astrophysics Source Code Library, ascl: **1408.004**  
 Okajima, T., Soong, Y., Balsamo, E. R., et al. 2016, *Proc. SPIE*, **9905**, 99054X  
 Osten, R. A., Brown, A., Ayres, T. R., et al. 2000, *ApJ*, **544**, 953  
 Osten, R. A., Hawley, S. L., Allred, J., et al. 2006, *ApJ*, **647**, 1349  
 Osten, R. A., & Wolk, S. J. 2015, *ApJ*, **809**, 79  
 Paudel, R. R., Barclay, T., Schlieder, J. E., et al. 2021, *ApJ*, **922**, 31  
 Prigozhin, G., Gendreau, K., Doty, J. P., et al. 2016, *Proc. SPIE*, **9905**, 990511  
 Pye, J. P., Rosen, S., Fyfe, D., & Schröder, A. C. 2015, *A&A*, **581**, A28  
 Reale, F. 2007, *A&A*, **471**, 271  
 Reale, F., Güdel, M., Peres, G., & Audard, M. 2004, *A&A*, **416**, 733  
 Reale, F., & Micela, G. 1998, *A&A*, **334**, 1028  
 Reep, J. W., & Knizhnik, K. J. 2019, *ApJ*, **874**, 157  
 Reep, J. W., Siskind, D. E., & Warren, H. P. 2022a, *ApJ*, **927**, 103  
 Reep, J. W., & Toriumi, S. 2017, *ApJ*, **851**, 4  
 Reep, J. W., Ugarte-Urra, I., Warren, H. P., & Barnes, W. T. 2022b, *ApJ*, **933**, 106  
 Remillard, R. A., Loewenstein, M., Steiner, J. F., et al. 2022, *ApJ*, **163**, 130  
 Ribas, I., Porto de Mello, G. F., Ferreira, L. D., et al. 2010, *ApJ*, **714**, 384  
 Rucinski, S. M., Walker, G. A. H., Matthews, J. M., et al. 2004, *PASP*, **116**, 1093  
 Sakurai, T. 2022, *Physi*, **5**, 11  
 Sasaki, R., Tsuboi, Y., Iwakiri, W., et al. 2021, *ApJ*, **910**, 25  
 Scargle, J. D., Norris, J. P., Jackson, B., & Chiang, J. 2013, *ApJ*, **764**, 167  
 Schaefer, B. E., King, J. R., & Deliyannis, C. P. 2000, *ApJ*, **529**, 1026  
 Schmitt, J. H. M. M., & Favata, F. 1999, *Natur*, **401**, 44  
 Shibata, K., & Yokoyama, T. 2002, *ApJ*, **577**, 422  
 Simões, P. J. A., & Kontar, E. P. 2013, *A&A*, **551**, A135  
 Telleschi, A., Güdel, M., Briggs, K., et al. 2005, *ApJ*, **622**, 653  
 Toriumi, S., & Airapetian, V. S. 2022, *ApJ*, **927**, 179  
 Toriumi, S., Schrijver, C. J., Harra, L. K., Hudson, H., & Nagashima, K. 2017, *ApJ*, **834**, 56  
 Tsuboi, Y., Imanishi, K., Koyama, K., Grosso, N., & Montmerle, T. 2000, *ApJ*, **532**, 1089  
 Tsuboi, Y., Koyama, K., Murakami, H., et al. 1998, *ApJ*, **503**, 894  
 Tsuboi, Y., Yamazaki, K., Sugawara, Y., et al. 2016, *PASJ*, **68**, 90  
 van den Oord, G. H. J., & Mewe, R. 1989, *A&A*, **213**, 245  
 Veronig, A. M., Brown, J. C., Dennis, B. R., et al. 2005, *ApJ*, **621**, 482  
 Virtanen, P., Gommers, R., Oliphant, T. E., et al. 2020, *NatMe*, **17**, 261  
 Warren, H. P., Winebarger, A. R., & Brooks, D. H. 2010, *ApJ*, **711**, 228  
 White, N. E., Culhane, J. L., Parmar, A. N., et al. 1986, *ApJ*, **301**, 262